

Reactor Neutrino Spectra

Anna C. Hayes,¹ and Petr Vogel²

¹T-2 Theoretical Division MS283, Los Alamos National Laboratory, Los Alamos, NM 8545, USA ; email: anna_hayes@lanl.gov

²Kellogg Radiation Laboratory 106-38, California Institute of Technology, Pasadena, CA 91125, USA ; email: pvogel@caltech.edu

Xxxx. Xxx. Xxx. Xxx. YYYY. AA:1–29

This article's doi:
10.1146/((please add article doi))

Copyright © YYYY by Annual Reviews.
All rights reserved

Keywords

Reactor, antineutrino, uranium, plutonium, oscillations, anomaly

Abstract

We present a review of the antineutrino spectra emitted from reactors. Knowledge of these and their associated uncertainties are crucial for neutrino oscillation studies. The spectra used to-date have been determined by either conversion of measured electron spectra to antineutrino spectra or by summing over all of the thousands of transitions that makeup the spectra using modern databases as input. The uncertainties in the subdominant corrections to beta-decay plague both methods, and we provide estimates of these uncertainties. Improving on current knowledge of the antineutrino spectra from reactors will require new experiments. Such experiments would also address the so-called reactor neutrino anomaly and the possible origin of the shoulder observed in the antineutrino spectra measured in recent high-statistics reactor neutrino experiments.

Contents

1. INTRODUCTION	2
2. NUCLEAR REACTORS AS ELECTRON ANTINEUTRINO SOURCES.....	3
3. THEORETICAL DETERMINATION OF THE REACTOR $\bar{\nu}_e$ FLUX AND SPECTRUM	7
3.1. Corrections to the β decay electron and $\bar{\nu}_e$ spectrum for the allowed β transitions.....	10
3.2. First forbidden β decays	14
4. DETECTOR REACTION $\bar{\nu}_e + p \rightarrow e^+ + n$	17
5. THE SHOULDER OR SO-CALLED "BUMP" IN REACTOR ANTINEUTRINO SPECTRA	18
6. THE REACTOR ANOMALY AND NEW EXPERIMENTS	23
7. UNCERTAINTIES IN THE ANTINEUTRINO SPECTRA	24
8. SUMMARY AND FUTURE DIRECTIONS.....	26

1. INTRODUCTION

Nuclear reactors are intense, pure, and controllable sources of low energy electron antineutrinos. They have been frequently, and very successfully, used in studies of fundamental neutrino properties. They will continue to play this role in the foreseeable future. It is, therefore, important to understand the corresponding $\bar{\nu}_e$ flux, its energy distribution, and the associated uncertainties in as much detail as possible. Here we review the work devoted to this issue.

The existence of neutrinos was suggested by Pauli already in 1930, in order to resolve the then apparent energy and angular momentum non-conservation in nuclear beta decay. Yet, the proof that neutrinos are real particles had to wait until 1953-1959, when Reines and Cowan (1, 2) detected the electron antineutrinos emitted by a nuclear reactor. That fundamental experiment was the beginning of the field of neutrino exploration using reactor antineutrinos.

The most important discovery in neutrino physics to-date is the existence of neutrino oscillations and by consequence the finite, albeit very small, rest mass of the neutrino. To explore oscillations with the early reactor experiments detectors were placed at distances $L \leq 100$ m (3, 4, 5, 6, 7, 8, 9, 10) and the observed $\bar{\nu}_e$ spectra were compared with that expected, the latter being based on the then accepted evaluation. Neutrino oscillations, i.e. variation of the spectrum with the distance from the reactor, were not observed in these short baseline experiments, in agreement with our present knowledge of the three-neutrino oscillation phenomenology. Later reactor experiments (11, 12, 13) at larger distances (~ 1 km) established an important upper limit for the mixing angle θ_{13} , showing that this mixing angle is substantially smaller than the other two mixing angles, θ_{12} and θ_{23} , the latter being reasonably well determined at that time. Interpretation of results from these pioneering experiments was directly dependent on knowledge of the reactor neutrino flux and spectrum.

More recent, and still running, reactor neutrino experiments (14, 15, 16, 17, 18) are devoted primarily to the determination of the mixing angle θ_{13} with the characteristic distance from the reactor of ~ 1 km, i.e., near the corresponding oscillation minimum. In order to avoid, or substantially reduce, dependence on detailed knowledge of the reactor spectrum, these experiments use two essentially identical detectors, with one or more placed relatively close to the reactors and the other one (or several) further away. By comparing the

signals at two distances it became possible to determine the oscillation signal corresponding to the angle θ_{13} with very good accuracy. The detectors employed in these experiments are substantially larger than those in the previous generation of experiments and, thus, the statistical accuracy of the spectrum determination is substantially better. Although not the original intent, these modern experiments provide a detailed test of the absolute reactor $\bar{\nu}_e$ flux and energy spectrum, and they raise new questions about our understanding of the expected spectra.

For precision reactor neutrino studies accurate knowledge of the reactor neutrino flux and spectrum is important. This issue became more pressing with the reevaluation of the spectra in 2011 in Refs. (19, 20), which resulted in the upward revision of the expected reactor antineutrino signal by $\sim 6\%$. These revisions suggested that all above mentioned experiments are missing approximately 6% of the signal, independent of the distance from the reactor, beginning at $L \geq 10$ m. This shortfall has become known as the “reactor anomaly” and it has been interpreted (21) as a possible indication of the existence of an additional, fourth, necessarily sterile, light neutrino of mass $O(1 \text{ eV})$, that becomes observable through subdominant mixing with the active neutrinos. If confirmed, this would be a discovery of fundamental importance. However, the sterile neutrino interpretation of the anomaly hinges on the accuracy of the expected reactor neutrino flux.

2. NUCLEAR REACTORS AS ELECTRON ANTINEUTRINO SOURCES

Nuclear reactors derive their power from the fission of U and Pu isotopes and from the radioactive decay of the corresponding fission fragments. The beta decay of the fragments is the source of the electron antineutrinos. The total antineutrino spectrum can be expressed as a sum over the spectra for the dominant fissioning actinides,

$$S(E_\nu) = \sum_i f_i \left(\frac{dN_i}{dE_\nu} \right), \quad (1)$$

where f_i is the number of fissions from actinide i and dN_i/dE_ν is the cumulative $\bar{\nu}_e$ spectrum of i normalized per fission. Thus, as a first step, the parameters f_i must be determined, which requires detailed information from the reactor operator, including the total thermal power and the linear combination of actinides contributing to the power. The total reactor thermal energy W_{th} and the parameters f_i are related through

$$W_{th} = \sum_i f_i e_i, \quad (2)$$

where e_i is the effective thermal energy per fission contributed by each actinide i . In power reactors 99.9% of the power comes from the fission of ^{235}U , ^{239}Pu , ^{241}Pu and ^{238}U , and only these isotopes are considered. The corresponding effective energies per fission are determined from the energy released in fission, minus the energy carried off by the antineutrinos, plus the energy produced by neutron captures on the reactor materials. The evaluated (22, 23, 24) energies, e_i , are given in Table 1. The corresponding estimated uncertainties are 0.25-0.5 %.

The data for W_{th} are usually available as function of time, while f_i , which are typically expressed as the relative fractions f_i/F , where F is the total number of fissions, are obtained by (often proprietary) simulations. The neutrino spectrum in eq. (1) can be expressed as

$$S(E_\nu) = \frac{W_{th}}{\sum_i (f_i/F) e_i} \sum_i \frac{f_i}{F} \left(\frac{dN_i}{dE_\nu} \right). \quad (3)$$

Table 1 Transforming the thermal power into the fission rate (all energies in MeV/fission). Columns 2-4 are from Ref. (22).

Nucleus	Energy from mass excess	Without ν	E_{TOT} including n-captures	E_{TOT} Ref. (23)	E_{TOT} in Ref.(24)
^{235}U	202.7 ± 0.1	192.9 ± 0.5	201.7 ± 0.6	$201.92\pm 0.46i$	202.36 ± 0.26
^{238}U	205.9 ± 0.3	193.9 ± 0.8	205.0 ± 0.9	205.52 ± 0.96	205.99 ± 0.52
^{239}Pu	207.2 ± 0.3	198.5 ± 0.8	210.0 ± 0.9	209.99 ± 0.60	211.12 ± 0.34
^{241}Pu	210.6 ± 0.3	200.3 ± 0.8	212.4 ± 1.0	213.60 ± 0.65	214.26 ± 0.33

In writing eq.(3) we are implicitly assuming that long-lived fission fragments not decaying in equilibrium have been corrected for. This issue is discussed in more detail below. There can also be contributions to the antineutrinos emitted from the reactor complex from the radioactive spent fuel stored there. This correction, which involves low-energy antineutrinos, is taken into account in oscillation experiments using inventory information supplied by the power company.

In order to determine the uncertainty in the $\bar{\nu}_e$ spectrum, it is necessary to determine the uncertainties in W_{th} and in f_i/F , as well as their correlations. The thermal power of a reactor is most accurately determined by temperature measurements in the coolant and the calculation of water flow rates and the energy balance around the reactor vessel or steam generator. It has been estimated, e.g. in Ref. (25) and in the references quoted there, that the total uncertainty can be as low as $\sim 0.5\text{-}0.7\%$, although more typically values of the order of 2% are quoted for W_{th} , and government regulations often allow a safety margin at this higher level.

Fuel management, i.e, fuel recycling and the repositioning of fuel rods within the reactor core, is quite reactor design specific. For example, CANDU reactors involve frequent recycling of fuel and the fuel composition f_i is kept close to constant. In pressurized water reactors, on the other hand, during each reactor cycle, which typically lasts about a year, the fuel composition is constantly changing; the ^{235}U is being depleted, Pu is being bred, and the Pu fission fraction is increasing. Though it represents the vast majority of the fuel, ^{238}U only contributes $\sim 10\%$ of the total fission because it is a threshold fission actinide, and the percentage of fissions from ^{238}U varies very slowly. The fraction of fissions from ^{238}U depends on the enrichment of the fuel and on the ratio of the thermal to fast neutron flux, which are two anti-correlated parameters in the reactor design. Fig. 1 shows the variation in the fuel fission fraction f_i/F as a function of burnup, GWdays per metric ton of in-going uranium fuel, which is equivalent to number of fissions. The left panel of this figure is for fresh 2.7% ^{235}U fuel. If the fuel enrichment is increased, the shape and magnitudes of the curves do not change significantly, rather the scale on the x-axis is expanded (right panel of Fig. 1), e.g., the burnup at which the fraction of fissions from ^{239}Pu overtakes that from ^{235}U is higher for higher enrichment.

In standard pressurized water reactors, at the end of each cycle about one-third of the fuel rods (those that have been burned for three cycles) are replaced with fresh fuel, and the position of many of the remaining partly burned rods is changed in order to keep the neutron flux across the reactor as close to flat as is possible. The average fuel composition as a function of time is simulated by detailed reactor burn codes, that often include a Monte Carlo treatment of the neutron transport. The codes are normally specific to the reactor

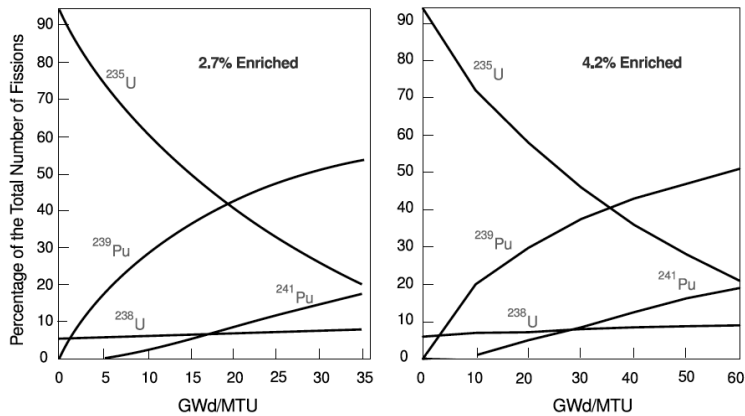


Figure 1

The evolution of the fuel composition for a pressurized water reactor over the reactor cycle, from Nieto *et al.* (26). The x-axis, GW-days per metric ton of in-going uranium fuel, is proportional to the number of fissions. As the fuel enrichment increases, the burn curves do not change significantly, rather the scale on the x-axis becomes expanded.

in question and checked and fine tuned by comparisons to spent fuel isotopics. For this reason, operators can quote the fractions f_i/F to higher accuracy than would be possible by independent untuned simulations, where isotopics of major actinides in spent fuel are reproduced at the $\sim 3\%$ level and that of fission fragments considerably less accurately. The magnitude of $\bar{\nu}_e$ spectra from the fission of different actinides are different, the total contribution per fission from ^{235}U is about 45% higher than from ^{239}Pu and about 60% lower than ^{238}U . Thus, the total antineutrino signal per fission can change during the reactor burn cycle. However, that variation is relatively small, and the uncertainty related to the uncertainties in f_i/F is less important than the uncertainty in the reactor thermal power W_{th} .

The typical variation in the antineutrino signal as a function of burnup for a pressurized water reactor is shown in Fig. 2. The data agree quite well with the prediction and the

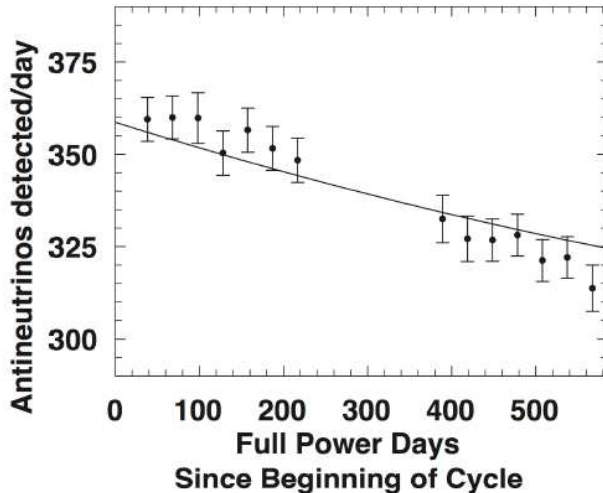


Figure 2

The change in the total number of antineutrinos emitted over the course of a reactor fuel cycle for a pressurized water reactor, resulting from the in-growth of ^{239}Pu , from Bowden *et al.* (27)

overall effect is an $\sim 10\%$ decrease of the count rate during a fuel cycle of about 550 days. This decrease, caused by the changes of the fuel composition, has to be quantitatively accounted for in oscillation experiments. Assuming that the reactor power or neutron flux is known independently, this change can also be used for remote monitoring of the operational status of a nuclear reactor. The issues determining the expected antineutrino spectra and their uncertainties for a declared burn history are key to the subfield of so-called “Applied Antineutrino Physics” (28), and they are clearly intimately related to the issues of this review. However, we will not discuss this application in any detail here.

In fission each actinide nucleus is split into two, usually unequal mass, fragments. In the case of ^{235}U , for example, the double hump mass fragment distribution peaks at $A = 94$ and 140 , respectively. The stable nuclei with those masses are ^{94}Zr and ^{140}Ce that have 98 protons and 136 neutrons together. The initial system has, however, 92 protons and 142 neutrons. To reach stability, therefore, six neutrons have to be transformed into six protons. That can be accomplished only by weak interaction β decays, in which six electrons and six electron antineutrinos are emitted. This is a general result for all reactor fuels; there are $\sim 6 \bar{\nu}_e$ per second emitted per fission, so a typical reactor emits $\sim 6 \times 10^{20}$ electron antineutrinos per each GW of the thermal energy power. The cascade of β decays of the fission fragments is a consequence of the general increase of the neutron to proton ratio

with increasing mass. The fission fragments, with masses near half of the initial nuclear mass, are neutron rich and hence they β decay, with a typical cascade of three decays each.

The β decays, the source of the reactor $\bar{\nu}_e$, are not instantaneous; they have finite lifetimes. As a consequence the spectrum requires certain time interval from the beginning of the fission process to reach a steady equilibrium. The time needed to reach equilibrium is different for $\bar{\nu}_e$ of different energies, typically being shorter for higher energies.

When using the reactor neutrinos to study neutrino oscillation, the neutrino capture on protons, $\bar{\nu}_e + p \rightarrow e^+ + n$ is almost exclusively used for neutrino detection. That reaction has a threshold, in the laboratory frame where the protons are at rest, $E_{thr} = [(M_n + m_e)^2 - M_p^2]/2M_p = 1.806$ MeV. Antineutrinos above this threshold mostly come from nuclei with relatively short half-lives that reach equilibrium within a few hours. However, there are some exceptions; there are six fission fragments with sizable fission yield, and $Q > 1.8$ MeV, ^{97}Zr , ^{132}I , ^{93}Y , ^{106}Ru , ^{144}Ce , and ^{90}Sr . The first three of them reach equilibrium within ~ 10 days, the next two have half-lives of 367 and 284 days, and ^{90}Sr has $T_{1/2} = 28.8$ years and decays into ^{90}Y with $Q = 2.28$ MeV. The effects of nonequilibrium is discussed in Ref. (29).

For ^{235}U above ~ 3 MeV of the neutrino energy equilibrium is reached within one day. However, at the detection threshold it takes about 100 days to reach 1% stability. When testing the spectra using shorter irradiation times it is therefore necessary to correct for such off equilibrium effects.

3. THEORETICAL DETERMINATION OF THE REACTOR $\bar{\nu}_e$ FLUX AND SPECTRUM

There are two complementary ways to determine the expected electron antineutrino spectrum of a nuclear reactor, the ‘*ab initio*’ summation and the electron spectrum conversion methods.

Assuming that the thermal power W_{th} , the normalized fission fractions f_i/F , and the energy per fission e_i of each fissioning isotope i are known or determined, the total $\bar{\nu}_e$ spectrum in eq. (3) requires detailed knowledge of the individual fission spectra dN_i/dE_ν for each of the four fuels (^{235}U , ^{238}U , ^{239}Pu , and ^{241}Pu). It is usually assumed that these individual spectra depend only on the nuclear properties of the fissioning isotopes and their fission fragments for thermal (0.025 eV) neutron fission in the case of ^{235}U , ^{239}Pu and ^{241}Pu , and fast fission for ^{238}U . This might not be completely accurate, since the fission fragment yields, i.e. the distribution of the fission fragments, depends to some extent on the reactor dependent energy shape of the neutron flux. Keeping this caveat in mind, we next discuss how the spectra dN_i/dE_ν are determined.

In the ‘*ab initio*’ approach the aggregate fission antineutrino spectrum is determined by summing the contributions of all β -decay branches of all fission fragments

$$\frac{dN_i}{dE_\nu} = \sum_n Y_n(Z, A, t) \sum_{n,i} b_{n,i}(E_0^i) P_{\bar{\nu}}(E_\nu, E_0^i, Z), \quad (4)$$

where $Y_n(Z, A, t)$ is the number of β decays of the fragment Z, A at time t , and the label n characterizes each fragment by whether it is in its ground state or an isomeric state. After sufficient burn time the quantity Y_n converges to the cumulative fission yield and is independent of time. Most fission fragments are produced by two mechanisms; first they are produced directly in the fission process with a so-called independent yield, and second

they are produced as the beta-decay daughter of a more neutron-rich fission fragment of the same mass number. The sum of the independent and beta-decay production of a fission fragment is its cumulative yield, and, once in equilibrium, the cumulative yield determines the contribution of a given fragment to aggregate fission antineutrino spectrum. The branching ratios $b_{n,i}(E_0^i)$ are characterized by the endpoint energies E_0^i . They are normalized to unity, $\sum_i b_{n,i}(E_0^i) = 1$, unless the fragment decays by an additional mode other than beta decay. Finally, the function $P_{\bar{\nu}}(E_{\bar{\nu}}, E_0, Z)$ is the normalized $\bar{\nu}_e$ spectrum shape for the branch n, i . An analogous formula holds for the corresponding aggregate fission electron spectrum, where $E_{\bar{\nu}}$ in the individual spectra P must be replaced by $E_e = E_0^i - E_{\bar{\nu}}$, since the nuclear recoil can be neglected within the accuracy considered here. Fig. 3 shows the antineutrino spectrum predicted by the summation method, using the JEFF-3.1.1 (30) database fission fragment yields and the ENDF/B-VII.1 (31) decay library. The ENDF/B-VII.1 decay library used here is that up-dated in ref. (32) to improve important issues with the older database pointed out in (33).

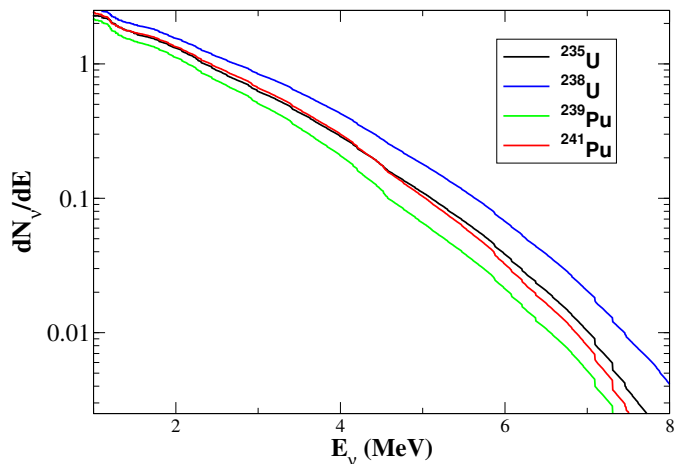


Figure 3

The antineutrino spectra for the four actinides determining the total antineutrino flux emitted from reactors. The fission yields were taken from JEFF-3.1.1 and the decay data, included the modeled data for unmeasured spectra, from ENDF/B-VII.1.

In applying the summation technique and eq. (4) several sources of uncertainty arise. The fission yields Y_n have been evaluated by several international database groups, but for many important fragments the yields involve large uncertainties. The branching ratios

$b_{n,i}$ are also not known for all fragments, and nor are the quantum numbers (spins and parity) of all of the initial and final states. The shape of the β decay spectrum P is well known for allowed transitions ($\Delta I \leq 1, \pi_i \pi_f = 1$) transitions. For neutron rich fission fragments all of the allowed transitions are Gamow-Teller transitions, determined by the operator $\sigma\tau$. However, $\sim 30\%$ of the transitions making up the aggregate spectra are known to be so-called first forbidden transitions, ($\Delta I \leq 2, \pi_i \pi_f = -1$), and involve nuclear structure dependent combinations of several more complicated operators. In the cases of some first forbidden operators, the spectra involve shapes that are noticeably different from those for allowed transitions, as described in the subsection 3.2. Finally, there are important, albeit small, corrections to the beta-decay spectra arising from radiative, nuclear finite size, and weak magnetism effects, and these can also depend on the details of the transition, as described in the subsection. 3.1. The difficulties of the ‘*ab initio*’ method, and the corresponding uncertainties are described in the next section and in the section on uncertainties.

The second method of determining the spectra dN_i/dE_ν begins with the experimentally measured aggregate *electron* spectrum associated with the fission of each individual actinide i . The electron spectrum for thermal neutron fission of ^{235}U , ^{239}Pu and ^{241}Pu were measured at ILL, Grenoble, France in 1980’s (34, 35, 36). The results were republished with a finer grid of electron energies recently in the Ref (37). ^{238}U fissions only with fast neutrons; its electron spectrum was measured much later at the neutron source FRMII in Garching, Germany (38). These experimentally determined electron spectra are automatically summed over all fission fragments and the corresponding β -decay branches, so no information on the fission yields and branching ratios is needed. It is necessary, however, to convert them into the $\bar{\nu}_e$ spectra. It is also necessary to make the relatively small correction for the fact that the electron spectra were determined before full equilibrium was reached.

To convert a measured aggregate electron spectrum into an antineutrino spectrum, the spectrum is binned over an energy grid, with the grid defining a set of virtual end-point energies E_0^i . The total aggregate spectrum is then fitted in terms of the amplitudes a_i for each virtual end-point energies, $dN_i/dE_e = \sum_i a_i P(E, E_0^i, Z)$. In principle, the position of the virtual end-point energies can also be part of the fit. Thus, the aggregate electron spectra, which have been measured in the energy window ($\sim 2 - 8.5$ MeV), are described by a sum of virtual β -decay branches of assumed spectral shapes. The conversion to the antineutrino spectrum is then simply accomplished by replacing the energy E_e in each branch by $E_0 - E_{\bar{\nu}}$. The procedure guaranties that the experimental electron spectrum is well reproduced. It is also straightforward to test whether the convergence on the number of energy intervals is achieved, which typically requires less than 30 intervals. However, the converted $\bar{\nu}_e$ depends to some degree on the assumptions made about the spectrum shapes P_i , whether they correspond to allowed or forbidden transitions, their Z dependence, and the form of the corrections arising from nuclear finite size and weak magnetism. An example of the uncertainty in the converted spectrum is shown in Fig. 4. There can also be some dependence on the endpoint energies E_0^i . To avoid sizable systematic errors when converting the electron spectrum it is necessary to use the data bases and evaluate the dependence of the average nuclear charge Z on the endpoint energy discussed in (20, 39).

A hybrid combination of these two methods has been also used (19), in which equation (4) is used for the fission fragments and β -decay branches where experimental data are available. Both electron and $\bar{\nu}_e$ spectra for this large subset of fission fragments are then evaluated. The difference between the measured electron spectrum (34, 35, 36) and the

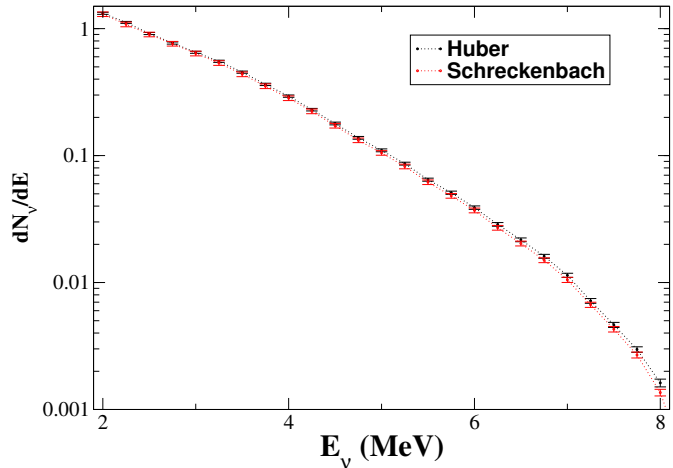


Figure 4

The antineutrino spectrum for ^{235}U derived by converting (20, 34) the measured (34) electron spectrum. The difference in the two derived spectra arises from differences in the assumptions made about the subdominant corrections to beta-decay. The uncertainty in the theoretical form of these corrections, discussed below and summarized in Table 3, are sufficiently large that direct experimental measurements will be necessary to determine the correct normalization of the antineutrino spectra to this accuracy.

evaluated partial electron spectrum is then converted into the $\bar{\nu}_e$ spectrum by the fitting procedure. This hybrid method has the advantage of taking account of the measured properties of a large subset of the fission fragments, and using experimental data to determine the energy dependence of forbidden transitions and the Z dependence of P_i .

In any of the methods, a necessary condition is a good understanding of the shape factors $P_{\bar{\nu}}(E_{\bar{\nu}}, E_0^i, Z)$ of the individual β decays, including nuclear charge Z and the end-points E_0^i , as well as the role of the allowed versus forbidden transitions.

3.1. Corrections to the β decay electron and $\bar{\nu}_e$ spectrum for the allowed β transitions

The β -decay spectrum shape can be expressed as

$$P_{\bar{\nu}}(E_{\bar{\nu}}, E_0^i, Z) = K p_e E_e (E_0 - E_e)^2 F(Z, E_e) C(Z, E_e) (1 + \delta(Z, A, E_e)) , \quad (5)$$

where K is the normalization factor (the function P must be normalized to unity when integrated over E_e and used in eq. (5)). $p_e E_e (E_0 - E_e)^2$ is the phase space factor, $F(Z, E_e)$ is the Fermi function that takes into account the effect of the Coulomb field of the daughter nucleus on the outgoing electron, and the shape factor $C(Z, E_e)$ accounts for the energy or momentum dependence of the nuclear matrix elements. For the allowed decays, $C(Z, E_e) = 1$. Finally, the function $\delta(Z, A, E_e)$ describes the subdominant corrections to the spectrum shape, to be discussed in detail below.

3.1.1. The Fermi Function. The Fermi function $F(Z, E_e)$ replaces the plane wave solution for the out-going electron with a Coulomb wave. It is straightforward to calculate F under the assumption of a point nuclear distribution, which leads to a Fermi function of the form,

$$F_0(Z, E_e) = 4(2p_e R)^{-2(1-\gamma)} \left[\frac{\Gamma(\gamma + iy)}{\Gamma(2\gamma + 1)} \right]^2 e^{\pi y}, \quad (6)$$

where $\gamma = \sqrt{1 - (\alpha Z)^2}$ and $y = \alpha Z E_e / p_e$. Here R is the cut-off radius, normally taken to be the radius of the nucleus in units of the electron Compton wavelength. The point Fermi function leads to a logarithmic divergence at $R = r = 0$ in eq.(6). Of course, for a nucleus with a finite charge radius the solution to the Dirac equation for the wave function of the out-going electron is finite everywhere.

3.1.2. The Finite Size Corrections. It is not possible to derive a general and exact correct for the finite size correction to the Fermi function. For this reason, different approximations have been made in the literature. These involve assumptions about the nuclear charge $\rho_{CH}(r)$ and weak isovector transition $\rho_W(r)$ densities, and perturbative expansions in $\alpha Z \left(\frac{ER}{\hbar c} \right)$ and/or in q^2 .

Holstein (40) derived an analytic expression using a first order expansion $\alpha Z \left(\frac{ER}{\hbar c} \right)$. The result depends on *both* the charge and weak densities. If the weak and charge densities are assumed to be the same $\rho_W = \rho_{CH}$ the finite size correction can be expressed (41) in terms of the first Zemach moment (42) $\langle r \rangle_{(2)}$, and is given in ref.(43) as,

$$\delta_{FS} = -\frac{3}{2} \frac{Z\alpha}{\hbar c} \langle r \rangle_{(2)} \left(E_e - \frac{E_V}{27} + \frac{m_e^2 c^4}{3E_e} \right) \quad (7)$$

The Zemach moment,

$$\langle r \rangle_{(2)} = \int d^3 r \rho_W(r) \int d^3 s \rho_{ch}(s) |\vec{r} - \vec{s}|, \quad (8)$$

is the first moment of the convoluted nuclear weak isovector transition density and electromagnetic ground state charge densities. Though the expression in eq. (7) is *exact* to order αZ , some assumption must be made about ρ_W and ρ_{CH} in calculating $\langle r \rangle_{(2)}$.

Behrens *et al.* (44) solved the finite size problem numerically, including higher order terms in αZ , but expanding the weak density ρ_W to first order in q^2 . The evaluation proceeds in two steps. First, the singularity at the origin in $F_0(Z, E_e)$ is removed by replacing it by the function $F(Z, E_e)$ based on the numerical solution to the Dirac equation for the outgoing electron in a finite size Coulomb potential, and evaluating it at $r = 0$

$$F(Z, E_e) = F_0(Z, E_e) \cdot L_0(Z, E_e) . \quad (9)$$

The functions L_0 , as well as $F(Z, E_e)$, are tabulated in (44). A less accurate, but much simpler analytic form of $F_0 L_0$, accurate to about 1% for $30 \leq Z \leq 70$ and $E_e \leq 8$ MeV, is available in (45). In the second step, in addition to using $F(Z, E_e)$ in place of $F_0(Z, E_e)$, the finite nuclear size correction needs to be added.

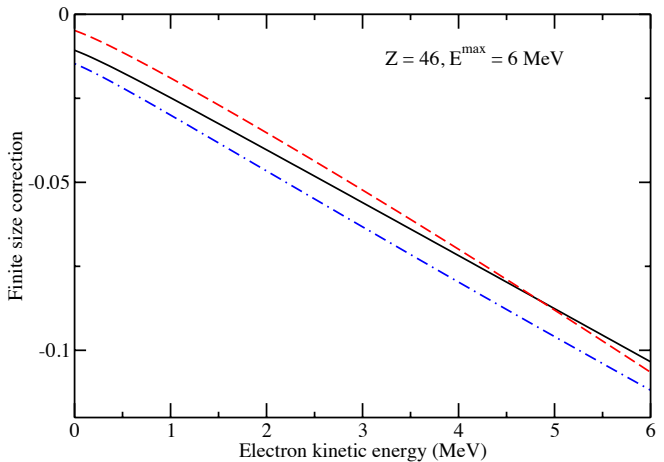


Figure 5

The finite size correction δ_{FS} for $Z = 46$ and maximum electron or $\bar{\nu}_e$ energy 6 MeV is plotted versus the electron kinetic energy. The full line is based on (43), the dashed line on (47) and the dot-dashed one on (48).

The two expansion methods, in αZ versus q^2 , lead to numerically similar results for uniform charge and weak density distributions of radius R , for which $\langle r \rangle_{(2)} = \frac{36}{35}R$, (41). In Ref. (43), uniform distributions were assumed and, ignoring constant terms independent of E_e , δ_{FS} becomes,

$$\delta_{FS}^{(1)} = -\frac{8}{5} \frac{Z\alpha R E_e}{\hbar c} \left(1 + \frac{9}{28} \frac{m_e^2 c^4}{E_e^2} \right) \quad (10)$$

An identical value for δ_{FS} was obtained for allowed transitions in ref. (46). In the latter reference it is noted that the magnitude of the finite size correction for uniform charge and weak densities is a factor of 1.3 smaller than that obtained assuming surface densities.

Terms that are higher order in αZ introduce small corrections that scale with R^2 , R/E_e and matrix elements of the operators $r^2[Y_2 \times \vec{\sigma}]$ and $\vec{\sigma} \times \vec{l}$. In ref. (47) the approximation of Behrens *et al.* is expressed in terms of an empirical analytic expression for allowed Gamow-Teller transitions. That formula was also applied in the reactor spectrum evaluation in

(20). A somewhat different but close formula was obtained in (48), where an average for a uniform or surface weak density distribution was estimated in terms of the matrix element ratio $\frac{\langle \sigma r^2 \rangle}{\langle \sigma \rangle R^2}$, and the finite size correction written as,

$$\delta_{FS}^{(2)} = -\frac{9}{10} \frac{Z\alpha R E_e}{\hbar c} \frac{\langle \sigma r^2 \rangle}{\langle \sigma \rangle R^2}. \quad (11)$$

For a uniform (surface) distribution $\frac{\langle \sigma r^2 \rangle}{\langle \sigma \rangle R^2} = 3/5$ (1). Ref. (19) followed this form and used $\delta_{FS}^{(2)} = -\frac{9}{10} \frac{Z\alpha R E_e}{\hbar c}$.

In Fig. 5 three of the different forms for the finite size corrections δ_{FS} that have been used in the literature for a uniform density are compared. Only the energy dependent part of δ_{FS} is plotted; the energy independent component is irrelevant for the normalized spectra. These differences, as well as the assumptions that must be made in evaluating $\langle r \rangle_{(2)}$, suggest that a large uncertainty needs to be assigned to δ_{FS} for allowed GT transitions.

3.1.3. The Radiative Corrections. The QED corrections of the first order in α to both the electron and $\bar{\nu}_e$ spectra in the β decay have been evaluated in Refs. (49, 50). An earlier version can be found in (51). Only the energy dependent corrections to the electron and $\bar{\nu}_e$ spectrum are relevant; only they affect the spectrum shape. They are of the form

$$\delta_{QED}^{\bar{\nu}} = \frac{\alpha}{2\pi} h(E_e, E_0), \quad \delta_{QED}^e = \frac{\alpha}{2\pi} g(E_e, E_0), \quad (12)$$

where $E_{\bar{\nu}} = E_0 - E_e$ and the functions $h(E_e, E_0)$ and $g(E_e, E_0)$ are defined in (49, 50). We note that for the conversion of the electron spectrum to the $\bar{\nu}_e$ spectrum only the difference $h(E_e, E_0) - g(E_e, E_0)$ is relevant.

3.1.4. The Weak Magnetism Correction. The interaction of the out-going electron with the magnetic moment of the daughter nucleus leads to a weak magnetism correction. The form of the correction is determined by the interference of the magnetic moment distribution of the vector current $\vec{J}_V = \vec{\nabla} \times \vec{\mu}$ with the spin distribution $\vec{\Sigma}$ of the axial current. Thus, there is *no* weak magnetism correction to Fermi or pseudo-scalar (0^-) transitions. In the non-relativistic approximation the correction depends on nuclear matrix elements of the operators $\vec{\sigma}$ and \vec{l} and for GT transitions has the form (40)

$$\delta_{WM} = \frac{4E_e}{3g_A M} \left(1 - \frac{m_e^2 c^4}{2E_e^2} \right) \left[\frac{\langle \vec{l} \rangle}{\langle \vec{\sigma} \rangle} + (\mu_p - \mu_n) \right], \quad (13)$$

where $\mu_p - \mu_n = 4.7$ is the nucleon isovector magnetic moment. In principle, the matrix element ratio $\frac{\langle \vec{l} \rangle}{\langle \vec{\sigma} \rangle}$ needs to be evaluated separately for each transition. As an approximation, one can use the truncated orbital current (43)

$$\delta_{WM} \approx \frac{4}{3} \frac{\mu_p - \mu_n - 1/2}{g_A M} E_e \left(1 - \frac{m_e^2 c^4}{2E_e^2} \right) \approx 0.5\% E_e / \text{MeV}, \quad (14)$$

An analogous weak magnetism correction, without the relatively small term $m_e^2/2E_e^2$, was suggested in (48) and used in (19, 20). In light nuclei it is possible to test the leading order term of weak magnetism correction δ_{WM} through its relation to the decay width of the $M1$ γ -ray transition for isobaric analog states. A list of these cases can be found in Ref. (20),

resulting in an average slope of $0.67 \pm 0.26\%$, in a fair agreement with the above formula. It is impossible, however, to test δ_{WM} for the transitions of real interest, i.e. for the β decay of fission fragments. The estimate above, therefore, must be assigned a sizable uncertainty.

The effect of the corrections on the electron and antineutrino spectra is summarized in Fig. 6. Since the spectrum for each fission fragment must be normalized to unity when integrated over all energies, the corrections increase the aggregate spectrum at some energies and lower it at other energies. In particular, below half the average end-point energy for all fission fragments, $\overline{E}_0/2$, the electron (antineutrino) spectrum is increased (decreased). Above $\overline{E}_0/2$, the electron (antineutrino) spectrum is decreased (increased). The approximate linear form of δ_{FS} and δ_{WM} in energy causes the decrease (increase) above $\overline{E}_0/2$ to also be approximately linear and to have a slope $\mp \frac{1}{2}(\delta_{FS} + \delta_{WM})$. A change in δ_{FS} or δ_{WM} to account for the uncertainties in these corrections would be directly reflected in a change in this slope. This point is important in assessing the statistical significance of the reactor anomaly, to be discussed later.

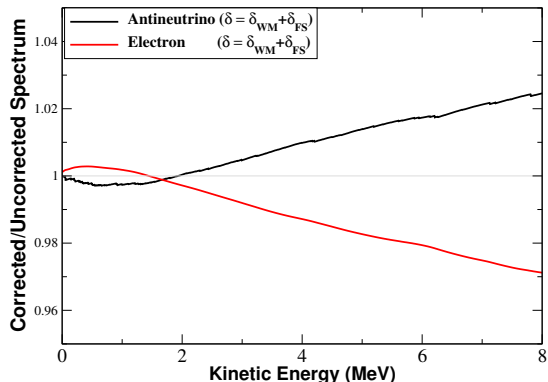


Figure 6

The finite size δ_{FS} and weak magnetism δ_{WM} corrections result in an approximately linear increase (decrease) in the antineutrino (electron) spectrum above half the average end-point energy $\overline{E}_0/2$. The figure shows the ratio of the spectra with and without these two corrections, using the summation method and the ENDF/B-VII.1 database. The form of the corrections used here are those given in eqs. (7) and (14), and the Z and A values involved are taken from the database.

3.2. First forbidden β decays

In the ground states of fission fragments the least bound protons and the least bound neutrons are often in states of opposite parity belonging to different oscillator shells. For

Table 2 The shape factors and leading-order weak magnetism corrections to allowed and first-forbidden decays from (43). The top panel is for Gamow-Teller transitions. The shape factors for allowed and first-forbidden Fermi beta decays are shown in the bottom panel. Nuclear operators \vec{J}_V and ρ_A are proportional to a nucleon velocity (p/M_N). CVC has been invoked to replace them by the analogous operators proportional to $E_0 r$ for \vec{J}_V , and a similar approximation has been made for the ρ_A operators proportional to (p/M_N). The weak magnetism correction for \vec{J}_V involves the unknown overlap of very different 1^- matrix elements and is therefore not listed. The nucleon isovector magnetic moment is $\mu_v = 4.7$, M_N is the nucleon mass, g_A is the axial vector coupling constant, and $\beta = p_e/E_e$.

Classification	ΔJ^π	Oper.	Shape Factor $C(E_e)$	Fractional Weak Magnetism Correction $\delta_{WM}(E_e)$
Gamow-Teller:				
Allowed	1^+	$\Sigma \equiv \sigma\tau$	1	$\frac{2}{3} \left[\frac{\mu_v - 1/2}{M_N g_A} \right] (E_e \beta^2 - E_\nu)$
1 st F.	0^-	$[\Sigma, r]^{0-}$	$p_e^2 + E_\nu^2 + 2\beta^2 E_\nu E_e$	0
1 st F. ρ_A	0^-	$[\Sigma, r]^{0-}$	λE_0^2	0
1 st F.	1^-	$[\Sigma, r]^{1-}$	$p_e^2 + E_\nu^2 - \frac{4}{3}\beta^2 E_\nu E_e$	$\left[\frac{\mu_v - 1/2}{M_N g_A} \right] \left[\frac{(p_e^2 + E_\nu^2)(\beta^2 E_e - E_\nu) + 2\beta^2 E_e E_\nu (E_\nu - E_e)/3}{(p_e^2 + E_\nu^2 - 4\beta^2 E_\nu E_e/3)} \right]$
Uniq. 1 st F.	2^-	$[\Sigma, r]^{2-}$	$p_e^2 + E_\nu^2$	$\frac{3}{5} \left[\frac{\mu_v - 1/2}{M_N g_A} \right] \left[\frac{(p_e^2 + E_\nu^2)(\beta^2 E_e - E_\nu) + 2\beta^2 E_e E_\nu (E_\nu - E_e)/3}{(p_e^2 + E_\nu^2)} \right]$
Fermi:				
Allowed	0^+	τ	1	0
1 st F.	1^-	$r\tau$	$p_e^2 + E_\nu^2 + \frac{2}{3}\beta^2 E_\nu E_e$	0
1 st F. \vec{J}_V	1^-	$r\tau$	E_0^2	-

this reason about 30% of all β decays contributing to the reactor neutrino spectrum are forbidden decays. The forbidden decays tend to be more prevalent in the higher energy part of the aggregate spectra, where the phase space advantage wins out over the suppression due to the forbiddenness of the transitions, the latter nominally scaling with $(pR)^2 \ll 1$.

The selection rules for the first forbidden β decays are $\pi_i \pi_f = -1$ and $\Delta J \leq 2$. In the leading order there are six relevant operators (43), which can be reduced in the number of independent operators by invoking the conserved vector current and relating operators proportional to $\vec{\nabla}/M\tau$ to the operator $\vec{r}\tau$. Two of the operators, γ_5 and $\vec{\alpha}$ involve emission of the $s_{1/2}$ electrons, and hence the corresponding shape factor $C(Z, E) = 1$, as is the case for allowed decay. However, the four additional operators involve the emission of the $p_{1/2}$ state electrons, and $C(Z, E) \neq 1$ in these cases. The shape factors $C(Z, E)$ for the six first forbidden operators are listed in Table 2.

In the case of $\Delta J = 2$, the unique first forbidden transition, only one operator can contribute, and corresponding shape factor is $C(Z, E) = p_e^2 + p_\nu^2$. For $\Delta J = 0$ two operators contribute and for $\Delta J = 1$ three. In general, the overall shapes factor $C(Z, E)$ of such transitions depends on the magnitude and sign of the matrix elements of the different forbidden operators contributing to the transition. The situation is often even more complicated since $|J_i - J_f| \leq \Delta J \leq J_i + J_f$ so that in typical decays of an odd-A or odd-odd nucleus more than one ΔJ contributes. For the even-even nuclei $J_i = 0$ and only one $\Delta J = J_f$ is relevant in that case

First forbidden β decays often exhibit spectra of similar shape to allowed decays. As pointed in ref. (52), this is likely the case whenever the Coulomb energy of the emitted

electrons is much larger than its total energy at the nuclear radius, $\alpha Z/R \gg E_0/m_e$, with R is expressed in the electron Compton wavelength units. This limit is often referred to as the ξ approximation, (52). However, taking as an example the important decay of ^{92}Rb with $\alpha Z/R = 19.2$, and $E_0 = 16.8m_e$, $\alpha Z/R \sim E_0$. For this and many of the high Q -value decays that dominate the aggregate spectra above 5 MeV, the ξ approximation cannot be used as guidance. Nevertheless, in the case of ^{92}Rb , at least, the measured β spectrum (53), dominated by the $0^- \rightarrow 0^+$ ground state branch, has essentially an allowed shape.

The QED or radiative corrections to the spectrum, δ_{QED} , depend only on the emitted electron energy. Hence δ_{QED} , defined in the eq. (12), is the same for forbidden transitions as it is for the allowed decays.

On the other hand, the weak magnetism corrections are operator dependent. They are listed for first forbidden transitions in ref. (43). As noted above, δ_{WM} vanishes for $\Delta J = 0$ operators. In particular, there is no weak magnetism correction for $0^- \rightarrow 0^+$ transitions, and such transitions represent an important component of the antineutrino spectra, especially at high energy. The weak magnetism correction also vanishes for the vector current (Fermi) operator \vec{r} , which is one of the operators responsible for the $\Delta J = 1^-$ transitions. Thus, in the absence of detailed calculations for the structure and combination of the matrix elements determining the 1^- transitions, the form of the weak magnetism correction that should be used is uncertain.

The finite size correction for the first forbidden β decays is a complicated and so far not a satisfactorily resolved issue. Ideally a simple correction in terms of a formula of δ_{FS} , analogous to that for the allowed GT decay in the eq. (10), would be applied to each transition of a given ΔJ . However, as in the case of the weak magnetism corrections, the finite size correction is operator dependent. Behrens *et al.* (44) addressed the problem by introducing corrections to the six basic operators, either in terms of additional radial integrals that have to be evaluated or as tabulated numerical corrections to the shape factors $C(Z, E)$ (54, 55). In one application (56), the first forbidden decays of ^{136}Te and ^{140}Xe were evaluated both using the shell model and QRPA, and the nuclear finite size found to result in a reduction of the neutrino flux above the 1.8 MeV threshold of 2-5 % depending on the E_0 , but to be operator and ΔJ dependent.

The lack of a comprehensive and/or single treatment for the nuclear size corrections for forbidden transitions, and its detailed dependence on the operators determining the transition, represents an important source of uncertainty in the aggregate fission antineutrino spectra.

The effect of the forbidden transition operator dependence on the deduced antineutrino spectrum using the conversion method has been examined in (43). The measured (34) aggregate electron fission spectrum for ^{235}U was fit assuming either all allowed transitions or various combinations of the allowed and forbidden operators listed in Table 2. Excellent fits to the electron spectrum were found in all cases, indicating that the electron spectrum cannot distinguish between these scenarios. However, the different treatments of the forbidden transitions lead to different antineutrino spectra, both in shape and magnitude at about the 4% level. Two examples, taken from (43), are shown in Fig.7, where in one case all transitions are assumed to be allowed, while in the second case the best fit results from about 25% forbidden decays. For the assumption of all allowed transitions, a systematic increase in the number of antineutrinos relative to Schreckenbach *et al.* (34) of about 2.5% was seen, while in the case that forbidden transitions were included no increase relative to that reference is found.

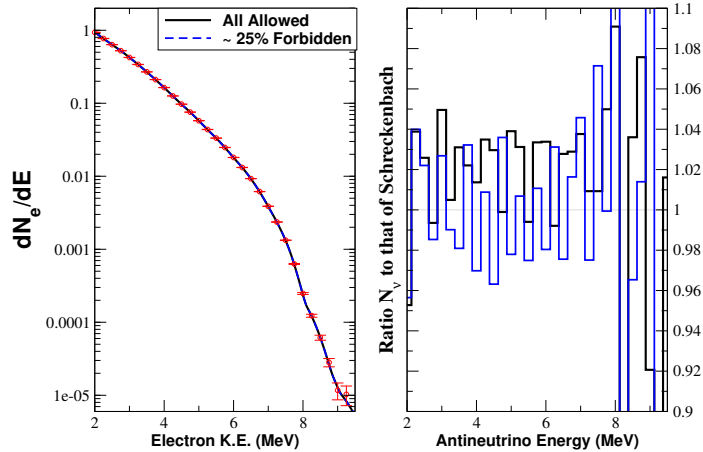


Figure 7

The fit to the electron spectrum for ^{235}U (left) for two different assumptions on how to treat forbidden transition, and the ratio of the corresponding antineutrino spectra to that of Schreckenbach *et al.* (34)(right). The electron spectrum are fit assuming (a) all allowed GT branches and (b) 25% forbidden transitions, and both δ_{FS} and δ_{WM} were included. When folded over the neutrino detection cross section the case for all allowed (25% forbidden) transitions results in a 2.5% (0.06%) increase in the number of detectable antineutrinos. Figure taken from (43).

4. DETECTOR REACTION $\bar{\nu}_e + p \rightarrow e^+ + n$

In essentially all experimental studies of reactor neutrino oscillations the $\bar{\nu}_e$ capture on protons is the detector reaction of choice, due to its relatively large cross section and the extremely convenient correlated signature of the positron emission followed by the delayed and spatially correlated neutron capture. Here we briefly review the corresponding cross section formulae. To zeroth order in $1/M$ the cross section is simply related to the neutron decay lifetime

$$\sigma_{tot}^{(0)} = \frac{2\pi^2/m_e^2}{fR\tau_n} E_e^{(0)} p_e^{(0)} \approx 9.52 \times 10^{-44} \left(\frac{E_e^{(0)} p_e^{(0)}}{\text{MeV}^2} \right) \text{cm}^2, \quad (15)$$

where $f^R = 1.7152$ is the neutron decay phase space factor that includes the Coulomb, weak magnetism, recoil and outer radiative corrections, but not the inner radiative corrections, and $E_e^{(0)} = E_\nu - (M_n - M_p)$.

However, even for the reactor energies the corrections of the first order in $1/M$ should be included (57)

$$E_e^{(1)} = E_e^{(0)} \left[1 - \frac{E_\nu}{M} (1 - v_e^{(0)} \cos \theta) \right] - \frac{\Delta^2 - m_e^2}{2M}, \quad (16)$$

where $\Delta = M_n - M_p$ and

$$\left(\frac{d\sigma}{d\cos\theta} \right)^{(1)} = \frac{\sigma_0}{2} \left\{ [(f^2 + 3g^2) + (f^2 - g^2)v_e^{(1)} \cos\theta] E_e^{(1)} p_e^{(1)} - \frac{\Gamma}{M} E_e^{(0)} p_e^{(0)} \right\}. \quad (17)$$

Here $f = 1$ and $g = 1.27$ are the nucleon form factors at $q^2 = 0$, $\sigma_0 = (G_F^2 \cos^2 \theta_C)/\pi(1 + \Delta_{inner}^R)$ and $\Delta_{inner}^R \sim 0.024$ is the inner radiative correction.

The quantity Γ is given by a somewhat cumbersome formula

$$\Gamma = 2(f + f_2)g[(2E_e^{(0)} + \Delta)(1 - v_e^{(0)} \cos \theta) - m_e^2/E_e^{(0)}] + (f^2 + g^2)[\Delta(1 + v_e^{(0)} \cos \theta) + m_e^2/E_e^{(0)}] + [(E_e^{(0)} + \Delta)(1 - \cos \theta/v_e^{(0)} - \Delta) \times [(f^2 + 3g^2) + (f^2 - g^2)v_e^{(0)} \cos \theta]]. \quad (18)$$

Here $f_2 = \mu_{anom} = 3.706$ is the nucleon isovector anomalous magnetic moment.

Various forms of extension to all orders in $1/M$ are given in (57, 58) as well as in the classic review (59), where, however the threshold behavior is not properly included. Radiative corrections of order α/π were evaluated, e.g. in (60). Their convenient numerical form given in (58) is

$$d\sigma(E_\nu E_e) \rightarrow d\sigma(E_\nu E_e) \left[1 + \frac{\alpha}{\pi} \left(6.00 + \frac{3}{2} \log \frac{M_p}{2E_e} + 1.2 \left(\frac{m_e}{E_e} \right)^{1.5} \right) \right]. \quad (19)$$

5. THE SHOULDER OR SO-CALLED “BUMP” IN REACTOR ANTINEUTRINO SPECTRA

All three recent large reactor experiments, Daya Bay, RENO, and Double Chooz (61, 62, 63), observed a feature (or shoulder) in the experimental spectrum at 4-6 MeV of the prompt positron energy, $E_{prompt} \approx E_\nu + (M_p - M_n - M_e) + 2M_e$, relative to the predicted theoretical evaluation in the Refs. (19, 20). The shoulder has not been observed in the measured fission electron beta-decay spectra (34, 35, 37, 38). It was also not observed in the previous test of the reactor spectrum shape (9). An example of the data, from the Daya Bay and RENO experiments, is shown in Fig. 8. In case of Daya Bay, the measured spectrum deviates from the predictions by more than 2σ over the full energy range and by 4σ in the range 4-6 MeV. The other two experiments (RENO and Double Chooz) report similar data and similar significance. The spectral shape of the shoulder cannot be produced by the standard L/E_ν neutrino oscillations dependence, independent of the possible existence of sterile neutrinos. In addition, it is too high in energy to be produced by antineutrinos emitted from neutron interactions with structural material in the reactor (65) or from the spent fuel. Its origin must be caused by the reactor fuel $\bar{\nu}_e$ emission.

In the context of the present review several questions need to be considered. What is the origin of this “bump”? Why was it not observed in the electron spectrum? Does its existence question expected/predicted reactor spectra in general?

The shoulder could have its origin in several effects that are not included, or not included accurately, in the reactor spectrum predictions (19, 20). Many of the important decays are

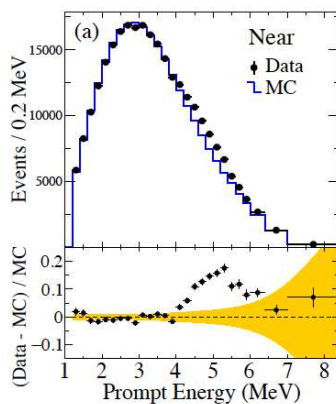
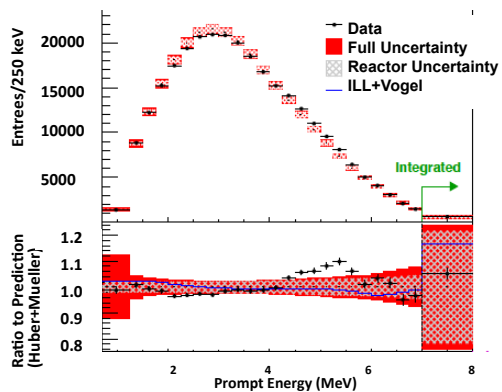


Figure 8

(Top) The shoulder (bump) observed in the near detector at Daya Bay (61), arising from the ratio of the observed spectrum to the predicted. The blue curve is the ILL prediction (34, 35) for ^{235}U and $^{239,241}\text{Pu}$ plus Vogel *et al.* (66) for ^{238}U . (Bottom) The shoulder observed (62) in the near detector at RENO. The predictions are from the Huber-Mueller model (20, 19) model, normalized to the same number of events.

forbidden, so that their shape factors and sub-dominant corrections might be different than assumed. Alternatively, the contribution of ^{238}U , that is only weakly constrained by the observed electron spectrum might not be accurate. The harder neutron spectrum in power reactors may lead to different fission fragment distributions than in the very thermal ILL reactor used for the electron fission spectra measurements (34, 35, 36). Finally, the measured electron spectra themselves (34, 35, 36), which represent the basis for the antineutrino evaluations (19, 20), might be incorrect.

The reactor $\bar{\nu}_e$ spectra are composed of β decays of hundreds of individual fission fragments, with ~ 6000 individual decay branches. However, at the relevant energies, 4-6 MeV of prompt energy, corresponding to ~ 4.8 -6.8 MeV $\bar{\nu}_e$ energy, relatively few (~ 10 -15) transitions determine 40-50% of the total spectrum, refs. (32, 64, 67), and they are mostly forbidden transitions. The other more numerous decays that determine the remainder of the spectrum in the bump energy window each contributes less than 2%. It is, therefore, possible that the conversion from the electron to the high-energy component of antineutrino spectrum involved an inaccuracy that resulted in a shoulder.

Several possible origins of the bump have been identified and investigated by different authors (67, 65), but it was generally concluded that, without further experimental investigation, it is impossible to determine which, if any or several, of the explanations are correct. However, several comments are in order, and we summarize the situation here.

Dwyer and Langford (67) used the *ab initio* summation method to construct the electron and antineutrino spectra from the ENDF/B-VII.1 fission yield and decay libraries, assuming allowed shapes and including the corrections discussed above. They observed that the ENDF/B-VII.1 library predicted a shoulder or “bump” very similar to that observed (61, 62, 63). In addition, they showed that a corresponding bump was predicted relative to the original measured (34, 35, 36) aggregate fission electron spectra. This explanation would, therefore, suggest that the measured electron spectra are incomplete, i.e. the shoulder was missed somehow in the measurements.

In the *ab initio* summation method the necessary input are the fission yields, and two standard fission-yields libraries, JEFF-3.1.1 and ENDF/B-VII.1 differ (65) significantly in the predicted yields of several nuclei dominating the shoulder region. In particular, the JEFF-3.1.1 library fission yields does not predict (65) a “bump” for the Daya Bay or RENO experiments, and agrees reasonably well with the measured electron spectra. A recent critical review (64) of the ENDF/B-VII.1 yields for ^{235}U uncovered erroneous yields for ^{86}Ge and all of its daughters, and showed that this error was generating excess of strength in both the predicted electron and antineutrino spectra at 5-7 MeV. When this problem was corrected, along with other less critical updates to the library, the predictions of the two databases are considerably closer, and agree within 6% at all energies. Most significantly, neither database (corrected ENDF or JEFF) now predict a bump relative to the measured ^{235}U aggregate electron fission spectrum, Fig. 9. Thus, at present, there is no evidence that the original measurements of the electron spectra are the origin of the bump.

An alternate source of the bump might lie with the conversion of the measured electron spectra to antineutrino spectra, which would point to the shoulder being produced by the approximations made for the corrections and/or for the forbidden transitions. However, this latter possibility can be mostly ruled out, (see ref. (65)), by examining the expected change in the bump region of spectrum for different treatments of the forbidden transitions. For example, three fission fragments that dominate in the bump region, ^{92}Rb , ^{96}Y and ^{142}Cs , all involve $0^- \rightarrow 0^+$ decays and, thus, have no weak magnetism correction. Since

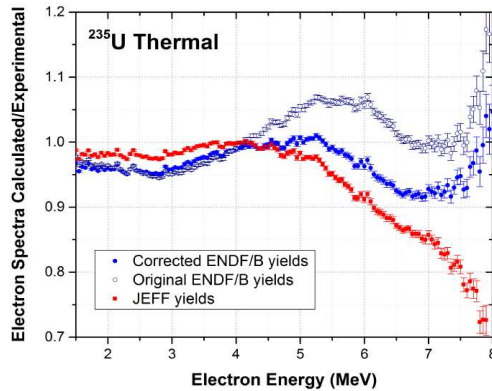


Figure 9

The ratio of the database predictions to the measured (34, 35) electron spectrum for ^{235}U . Neither JEFF nor the corrected ENDF/B database predicts a bump relative to the measured electron spectrum. Figure reproduced with the permission of A. Sonzogni *et al.*

the weak magnetism correction is opposite in sign to the finite size correction, a proper treatment of weak magnetism is important. There are two $\Delta J = 0^-$ operator, one GT and one proportional to the axial charge ρ_A , each with different shape factors, $C(E_e)$. Thus, there is considerable uncertainty as to how to treat these transition. To test this no weak magnetism and no shape correction was applied in one case to these three transitions and. In the second case no weak magnetism and the shape correction for a purely GT 0^- . The first treatment leads to a small increase in the antineutrino spectrum above about 4 MeV, which is a maximum of 1% at 8 MeV, while the second leads to a suppression in the energy region of interest. Thus, it was concluded in ref. (65) that a proper treatment of weak magnetism for forbidden transitions cannot account for a significant fraction of the shoulder.

At present, the two most likely sources of the bump seem to be ^{238}U or the hardness of the neutron spectrum. In the case of ^{238}U , there are a few observations worth commenting on. First, ^{238}U represents about 12% of the total fissions at RENO, compared to 7.6% and 8.7% at Daya Bay and Double Chooz, respectively, and the bump seen at RENO is larger than in the other two experiments. Also, the ^{238}U spectrum is considerably harder in energy than that of the other actinides, which results in ^{238}U contributing about 24% (15%) of the spectrum in the bump region for RENO (Daya Bay). Second, *both* the ENDF/B-VII.1 and JEFF-3.1.1 libraries predict a bump relative to the ^{238}U antineutrino spectrum of Mueller (19) and of the recent measurement of Haag (38), as shown in Fig. 10. Thus, without experiments designed to isolate the contributions from each actinide to the shoulder, ^{238}U

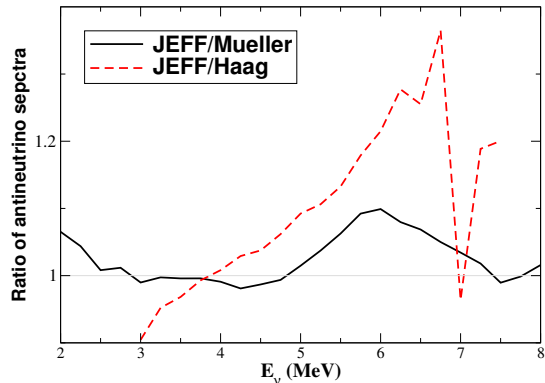


Figure 10

The ratio of the JEFF-3.1.1. antineutrino spectrum for ^{238}U to that of Mueller (19) and Haag (38). As can be seen, JEFF predicts a bump relative to the predictions of both Mueller and Haag, with the latter bump being the larger. Double Chooz use the Haag ^{238}U antineutrino spectrum, and JEFF-3.1.1 predicts a bump relative to Double Chooz, see ref. (65)

cannot be ruled out as a significant source of the bump.

Finally, the effect of the hardness of reactor neutron spectrum on the antineutrino spectrum has never been tested directly. The databases generally predict this to be a small effect. Nonetheless, the PWR reactors used by Daya Bay, RENO and Double Chooz are harder in energy than the thermal spectrum of the ILL reactor, and involve considerably larger epithermal components. In the epithermal energy region the fission yield distributions can be resonance dependent (68). If epithermal fission is a significant source of the bump, one might expect it to be most pronounced in ^{239}Pu , since there the first epithermal fission resonance at $E_n=0.32$ eV is quite isolated and strong, and it can account for as much as 25% of the total plutonium fission in some pressurized water reactors. Thus, any experimental tests of the variation of the yields of the dominant fission fragments with neutron energy would be very valuable in addressing this issue.

The existence of the “bump” has little effect (69) on the extraction of the neutrino oscillation parameters from the reactor experiments. In addition, it could be entirely uncorrelated with the “reactor anomaly”. However, it raises the very serious question of how well the antineutrino spectra are known, and suggests that estimated uncertainties at the 1-2% are too optimistic.

6. THE REACTOR ANOMALY AND NEW EXPERIMENTS

The total yield of $\bar{\nu}_e$ capture on protons measured in all past reactor experiments is lower than the predictions of Refs. (19, 20), a finding which is generally referred to as the “reactor neutrino anomaly”. The present status is illustrated in Fig. 11 where the older data are shown, together with the more recent high statistics result from the Day-Bay experiment (61). For the Daya-Bay experiment alone the ratio of the measured to expected yield is 0.946 ± 0.022 . A global fit, that includes all past measurements, results in the ratio $R = 0.942 \pm 0.009(\text{exp}) \pm 0.025(\text{model})$, when corrected for the known neutrino three-flavor oscillations. The average value of R is well determined, and the experimental uncertainty is substantially smaller than the model uncertainty assumed in (19, 20). Taking the quoted uncertainty in the model predictions at face value, the global value of R suggests reactor $\bar{\nu}_e$ disappearance as close as $L < 10$ m. Such short baseline disappearance cannot be accommodated within the standard $3 - \nu$ mixing model, and hence the phrase ‘reactor anomaly’.

The reactor anomaly is one of several experimental results that contradicts the standard three-flavor neutrino oscillation paradigm. Other experiments, including LSND (70), MiniBooNE (71), SAGE (72) and GALLEX (73), indicate non-standard ν_e disappearance or $\nu_\mu \rightarrow \nu_e$ appearance, albeit with the statistical significance of only $\sim 3\sigma$. The common feature of such anomalies is that the parameter $L(\text{m})/E_\nu(\text{MeV})$ is of the order of unity, and this similarity in L/E_ν has led to a proposed explanation involving one or more additional neutrino types, i.e., sterile neutrinos. Clearly, this is an issue of fundamental importance, potentially a source of the long sought after “physics beyond the standard model”.

It is beyond the scope of the present review to describe all of the experiments that comprise the current neutrino anomalies and their interpretation. However, detailed discussions, including a description of the experiments and their analyses, are provided in Refs. (74, 75). The possible existence of sterile neutrinos has to be confirmed or ruled out with new experiments, and a comprehensive discussion of the issue is provided in the white paper (76). Here we concentrate on aspects of the problem related to reactor neutrinos, where the experimental data are quite firm, but the expectations depend on an assumed reactor spectrum, involving uncertainties that are difficult to determine reliably. These uncertainties and the associated complications are discussed in a separate section of this article.

Quite generally, $|\Delta m_{i,j}^2(\text{eV}^2)| \cong 2.48 E_\nu(\text{MeV})/L_{osc}(\text{m})$. Thus, $L/E_\nu \sim 1$ implies $\sim \Delta m_{i,j}^2$ of a few eV^2 and the corresponding additional neutrino (or neutrinos), if they exist, must have the mass $m_{sterile} \sim 1$ eV, assuming that $m_1, m_2, m_3 \ll m_{sterile}$. The analysis in (75) restricts $\Delta m_{4,1}^2$ to the interval 0.8 - 2.2 eV^2 . The extra sterile neutrinos would have experimental consequences and their existence would be observable only if they mix with the active neutrinos. If sterile neutrinos are indeed responsible for current anomalies in neutrino physics, the corresponding mixing angle is $\sin_{new}^2 2\theta \sim 0.1$, with a range of about 0.06 - 0.22.

To test the short baseline oscillation sterile neutrino hypothesis it is necessary to perform experiments sensitive not only to the total flux, but more importantly to the oscillation pattern in E_ν or L . For reactors this translates into the distance between the neutrino source and the detector being between ~ 1 -15 meters; at larger distances the oscillatory behavior would be washed out. The statistical and systematic uncertainties of new experiments have to be at the level of few percent for a definitive result. A number of reactor experiments that fulfill these criteria have been proposed. They are at different stages of planing, funding,

and construction. The same sterile neutrino hypothesis can be also tested with strong radioactive sources at similar distances or with accelerator neutrinos at proportionally larger distances, and there are also a number of proposed experiments of this type.

The new reactor experiments, with planned high statistics and low systematic uncertainties, would also provide very significant and valuable tests of the reactor antineutrino spectrum in general. Some of the experiments will use research reactors based on the highly enriched ^{235}U fuel, and have the additional advantage of a compact-sized reactor core. Thus, the ^{235}U spectrum can be isolated and well-determined, and if statistics are good enough, the “bump” feature explored. Experiments are planned at highly thermal neutron flux reactors and at higher neutron temperature reactors, and comparisons between these will be important in shedding light on the role of epithermal neutrons in determining the antineutrino spectrum. When combined with the results from power reactors it should be possible to isolate the spectra of the other reactor fuels to much better accuracy that is currently possible. The results of such tests would also benefit the Applied Antineutrino Physics (27) aimed at monitoring reactor operations and fuel content.

Multiple very short-baseline reactor (VSBR) experiments are described together in Refs. (77, 78). They have been proposed globally; in the US (PROSPECT, NuLat), Belgium (SoLid), France (NUCIFER, STEREO), Russia (DANSS, NEUTRINO-4, POSEIDON), and Korea (HANARO). Generally, since the VSBR experiments are at shallow depth, and necessarily near the reactor cores, control of the backgrounds is a challenging task. The detectors are usually Gd loaded or ^6Li loaded liquids. While the Gd-liquid scintillator technology is mature, the ^6Li has the advantage that the neutron capture produces an α particle and triton. This provides a good localization of the delayed signal and additional pulse-shape discrimination. Within few years of data taking, the parameter region suggested by the anomalies should be well-covered and the experiments should be in a position to make definitive statements on the possible existence of light sterile neutrinos.

7. UNCERTAINTIES IN THE ANTINEUTRINO SPECTRA

For many neutrino oscillation analyses the uncertainties in the expected antineutrino spectra are as important as the spectra themselves. As discussed above, the expected spectra can be derived by two main methods, by summing all of the individual transitions that make up the spectrum using the nuclear databases as input, or by converting a measured aggregate fission electron spectrum to an antineutrino spectrum. The issues determining the uncertainties are somewhat different in the two case.

The summation method requires knowledge of both the decay spectra and fission yields for all of the fragments determining the spectra, and both inputs involve uncertainties. For the decay of individual nuclei, the databases are incomplete because about 5% of the nuclei are sufficiently far from the line of stability that no measurements of the spectra are available. Thus, summation methods must rely on some modeling to account for the missing spectra. A model for the spectrum of each missing nucleus is provided by ENDF in terms of a continuous spectrum, which is derived from nuclear structure calculations. The model (88, 89) is an extension of the Finite-Range Droplet Model plus Quasi-particle Random Phase Approximation, tuned to account for the so-called pandemonium effect (90) (viz., a very large number of low-energy beta decays to the many high-lying excited states of the daughter) as well as forbidden transitions, and is supplemented by the nuclear structure library ENSDF (91) where appropriate.

For many of the nuclei with decay measurements, the decay schemes are uncertain and the spin and parity ΔJ^π involved in the transition is unknown for many branches. In addition, since about 30% of the transitions are forbidden, the finite size δ_{FS} and weak magnetism δ_{WM} corrections and the shape factors $C(E, Z)$ applied to these transitions must be assigned large uncertainties. For all forbidden transitions the finite size has been approximated to-date.

The radius determining the finite size correction involves both the weak transition density ρ_W and the charge density ρ_{ch} . Under the assumption that $\rho_W = \rho_{ch}$, we recover eq. (7). However, the radius describing the finite size corrections is nuclear structure dependent. Several density or radius approximations have been made in the literature (92, 93, 94), and these differ from one another by about 50%. Thus, we place a 50% uncertainty on the allowed finite size correction. For forbidden transitions, a general analytic expression for the form of the finite size corrections has not been derived. A treatment to leading order in q^2 has been derived in (44), but it involves calculating several nuclear structure dependent matrix elements. Thus, we place a 100% uncertainty on the finite size correction to forbidden transitions.

The weak magnetism correction also involves some uncertainty. There are two-body meson-exchange current corrections that are nuclear structure dependent. These are typically of the order of 10-20% corrections. In addition, as the weak magnetism correction involves matrix elements of both σ and ℓ , and, in the absence of detailed nuclear structure calculations, some assumption must be made about $\langle \ell \rangle$. For the allowed and uniquely forbidden weak magnetism corrections we assign a correction of 20%. For the non-unique forbidden 1^- transitions we suggest an uncertainty of 25% to take account of the fact that δ_{WM} depends on the operator. In the case of $\Delta J = 0^-, 1^-$, more than one shape factor can contribute and the combination is nuclear structure dependent. Based on comparisons of the total antineutrino spectra computed using different choices of these $C(E, Z)$, we estimate the uncertainty to be about 30%.

The database fission yields are also uncertain for many important nuclei, and differences (65) between the JEFF-3.1.1 and ENDF/B-VII.1 evaluated yields of these nuclei were found to be as much as 20-50%. A more recent review and revision of the important fission yield in the ENDF/B-VII.1 database by Sonzogni *et al.* (64) has brought antineutrino spectrum predicted for ^{235}U by JEFF and ENDF databases to within better than 6% of each other over most all of the energy range relevant to reactor neutrino experiments. The two databases do deviate significantly between $E_\nu = 7-8$ MeV, but this energy window represent only a small fraction of the observed total. Up to about 4.5 MeV, ENDF/B is lower than JEFF, but above this energy JEFF drops steadily, becoming more than a factor of 1.5 lower than ENDF/B. Both databases are lower than the measured antineutrino spectrum for ^{235}U over the energy range $E_e = 1.5 - 7.5$ MeV, although this may reflect the need to further correct the databases for the so-called pandemonium effect. While it is difficult to estimate the uncertainty in the database fission yields, we tentatively place the uncertainty arising from their contribution to the summation method at $\sim 10\%$, motivated in part by the good comparisons to decay-heat (95) and the work of (64).

Though many of the uncertainties in Table 3 also apply when converting a measured electron spectrum to an antineutrino spectrum, the situation is somewhat different. This is because the fit must reproduce the electron spectrum, even if the finite size correction is changed by, say, 50%. In ref. (43) different assumptions were made about which weak magnetism and shape factors should be applied to the non-uniquely forbidden component

Table 3 The estimated uncertainties for the ingredients that make up the aggregate antineutrino spectra when the summation method is used. These estimates are subjective and are based on the educated guess of the authors. They do not represent statistical variances.

Quantity	type	ΔJ^π	uncertainty
Unknown branching and J^π	allowed and forbidden	all	50%
Finite size corr.	allowed	1^+	50%
Finite size corr.	forbidden	$0^-, 1^-, 2^-$	100%
Weak magnetism	allowed	1^+	20%
Weak magnetism	forbidden	0^-	0
Weak magnetism	forbidden	2^-	20%
Weak magnetism	forbidden	1^-	25%
Shape factor	allowed	1^+	0
Shape factor	forbidden	2^-	0
Shape factor	forbidden	$0^-, 1^-$	30%
Fission yields	allowed and forbidden	all	10%
Missing spectra	allowed and forbidden	all	50%

of the spectrum and with fits to the electron spectrum of equal statistical accuracy, the antineutrino spectrum was found to vary by 4%. In the latter work, only expressions listed in Table 2 were used for δ_{WM} and $C(E, Z)$, i.e., no uncertainty was included. In addition, the finite size correction was kept as in eq. (7). To determine the full effect of the uncertainties that apply to a conversion from a measured electron spectrum to an antineutrino spectrum, listed in Table 3 (not including the last two listings), requires a detailed multi-parameter sensitivity study. In the absence of such a study, we tentatively place a 5% uncertainty on the conversion method.

8. SUMMARY AND FUTURE DIRECTIONS

Nuclear reactor neutrino experiments have played a central role in neutrino physics since the 1950s. Despite the complexity of the spectra of antineutrinos emitted from reactor, namely, that they result from thousands of beta-decay branches of unstable fission fragments, the spectra were determined reasonably accurately already in the 1980s. However, today’s neutrino oscillation studies have reached a precision such that there is a need to know the spectra to much higher accuracy, i.e., to considerably better than 5%. For example, the reactor neutrino anomaly which suggests the existence of a ~ 1 eV sterile neutrino, represents a 6% discrepancy between expected and observed number of detected antineutrinos in all short baseline experiments. The total signal rate is experimentally determined to better than 1% accuracy. The statistical significance of the discrepancy, however, crucially depends on the uncertainty in the expected spectra.

In this review we have attempted to summarize the experiments and models that have constituted the “expected” spectra and how these have evolved over the years. Determining the uncertainties in the expected spectra is quite difficult and there are many issues involved. In general, conversion of measured aggregate electron fission spectra provide more accurate determinations of the antineutrino spectra than do predictions from the databases. The database calculations do, however, provide a very important means of estimating the relative importance of theoretical corrections to the spectra and their uncertainties. In examining

these and the underlying theories used to derive the corrections, we estimate that the uncertainty in antineutrino spectra derived by the conversion method are about 5%. The uncertainties in the summation method are considerably worse and at least in the upper part of the antineutrino spectrum are probably up to the 20% level. We emphasize that these are our subjective estimates. They are based on educated guesses and they do not represent statistical variances.

Improving on the theoretical inputs to the spectra will be challenging. Thus, there is a clear need for new experiments. Ideally, these should involve more than one reactor design and fuel enrichment, because the remaining issues will require a better understanding of the role of the hardness of the reactor neutron spectrum and of the four individual actinides that make up total spectra. For the bump energy region, better measurements of the ^{238}U spectrum would be particularly valuable.

ACKNOWLEDGMENTS

Anna Hayes thanks the LDRD program at Los Alamos National Laboratory for partial support for this work. Petr Vogel thanks the Physics Department at the California Institute of Technology for partial support for this work. They both thank Jim Friar, Gerry Garvey, Alejandro Sonzogni, Libby McCutchen, Jerry Jungman, and members of the Daya Bay, Double Chooz, and RENO experimental teams for valuable discussions.

LITERATURE CITED

1. Reines F. and Cowan C. L., Jr. *Phys. Rev.* 92:830 (1953)
2. Reines F. and Cowan C. L., Jr. 1959, *Phys. Rev.* 113:273 (1959)
3. Kwon H. et al. *Phys. Rev. D* 24:1097 (1981)
4. Zacek G. et al. *Phys. Rev. D* 34:2621 (1986)
5. Alfonin A. I. et al. *JETP* 67:213 (1988)
6. Vidyakin G. S. et al. *JETP* 59:390 (1994)
7. Declais Y. et al *Phys. Lett.* B338:383 (1994)
8. Achkar B. et al. 1995, *Nucl. Phys.* B434:503 (1995)
9. Achkar B. et al. 1996, *Phys. Lett.* B374:243 (1996)
10. Greenwood Z. D. et al. *Phys. Rev. D* 53:6054 (1996)
11. Apollonio M. et al. *Phys. Lett.* B466:415 (1999)
12. Boehm F. et al. *Phys. Rev. Lett.* 84:3764 (2000)
13. Boehm F. et al. *Phys. Rev. D* 62:072002 (2000)
14. An F. P. et al. *Phys. Rev. Lett.* 108:171803 (2012)
15. An F. P. et al. *Phys. Rev. Lett.* 112:061801 (2014)
16. Ahn J. K. et al. *Phys. Rev. Lett* 108:191802 (2012)
17. Abe Y. et al. *Phys. Rev. Lett* 108:131801 (2012)
18. Abe Y. et al. *Phys. Lett.* B735:51 (2014)
19. Mueller T. A. et al. *Phys. Rev. C* 83:054615 (2011)
20. Huber P. *Phys. Rev. C* 84:024617 (2011); erratum *ibid.* 85:029901 (2012)
21. Mention G. et al. *Phys. Rev. D* 83:073006 (2011)
22. James M. F. *J. Nucl. Energy* 23:517 (1969)
23. Kopeikin V. , Mikaleyan L. and Sinev V. . *Phys. Atom. Nucl.* 67:1892 (2004)
24. Ma X.B., Zhong W.L., Wang L.Z., Cjen Y.X., and Cao J., *Phys. Rev. C* 88, 014605 (2013).
25. Djurcic Z. et al. *J. Phys. G.* 36:045002 (2009)

26. Nieto M. M., Hayes A. C., Wilson W.B., Teeter C. M., and Stanbro W.D., *Nucl. Sci. and Eng* 149:(2004)
27. Bowden N. S. et al. *J. Appl. Phys.* 105:064902 (2009)
28. Bernstein A. et al. *Science & Global Security* 18:127 (2010); arXiv:0908.4338
29. Kopeikin V. I. , Mikaleyan L. A. and Sinev V. V. *Phys. Atom. Nucl.* 64:849
30. Kellett M.A. , Bersillon O., Mills R.W., “The JEFF-3.1/-3.1.1 Radioactive Decay Data and Fission Yields Sub-Libraries,” JEFF Report 20, NEA Report No. 6287 (2009).
31. Chadwick M.B., *Nucl. Data Sheets* **112**, 2887 (2011).
32. Sonzogni A. A., Johnson T. D. and McCutchan E. A. *Phys. Rev. C* 91:011301(R) (2015)
33. Fallot M. et al. *Phys. Rev. Lett.* 109:202504 (2014)
34. von Feilitzsch F., Hahn A. A. and Schreckenbach K. *Phys. Lett* 118B:365 (1982)
35. Schreckenbach K. et al. *Phys. Lett* 160B:325 (1985)
36. Hahn A. A. et al. *Phys. Lett* 218B:365 (1989)
37. Haag N. et al. *arXiv* 1405.3501 (2014)
38. Haag N. et al. *Phys. Rev. Lett* 112:122501 (2014)
39. Vogel P. *Phys. Rev. C* 76:025504 (2007).
40. Holstein B. R., Shanahan W. and Treiman S. B. *Phys. Rev. C* 5:1849 (1972)
41. Friar J.L., *Ann. Phys. (N.Y.)* 122, 151 (1979).
42. Zemach A.C., *Phys. Rev.* 104:1771 (1956)
43. Hayes A.C. et al. *Phys. Rev. Lett* 112:202501 (2014)
44. Behrens H. and Jänecke J. *Landolt-Börnstein Tables, Gruppe I, Band 4, Springer, Berlin* (1969), and
Behrens H. and Bühring W., *Electron Radial Wave Functions and Nuclear Beta-decay* (Clarendon Press, Oxford, 1982).
45. Schenter G. and Vogel P. *Nucl. Sci. Eng.* 83:393 (1983)
46. Holstein B. R. *Phys. Rev. C* 9:1742 (1974)
47. Wilkinson D. H. *Nucl. Inst. Meth* A290:509 (1990)
48. Vogel P. *Phys. Rev. D* 29:1918 (1984)
49. Sirlin A. *Phys. Rev. D* 84:014021 (2011)
50. Sirlin A. *Phys. Rev.* 164:1767 (1967)
51. Batkin I. S. and Sundaresan M. K. *Phys. Rev. D* 52:5362 (1995)
52. Weidenmüller H. A. *Rev. Mod. Phys* 33:574 (1961)
53. Rudstam G. et al. *At. Data Nucl. Data Tables* 45:239 (1990)
54. Suzuki T. et al. *Phys. Rev. C* 85:015802 (2012)
55. Zhi O. et al. *Phys. Rev. C* 87:025803 (2013)
56. Fang D-L. and Brown B. A. *Phys. Rev. C* 91:025503 (2015)
57. Vogel P. and Beacom J. F. *Phys. Rev. D* 60:053003 (1999)
58. Strumia A. and Vissani H., *Phys. Lett* B564:42 (2003)
59. Llewellyn Smith C. H., *Phys. Rep.* 3:261 (1972).
60. Kurylov A., Ramsay-Musolf M. J. and Vogel P. *Phys. Rev. C* 67:035502 (2003)
61. An P.F., *et al.*, arXiv:1508.04233v1 (2015).
62. Seo S-H. *Neutrino 2014, AIP Conf. Proc., E. Kearns and G. Feldman ed.* p. 080002 (2015), and J.H. Choi, *et al.*, arXiv:1511.05849v2 (2015).
63. Crespo-Anadon J. I. arXiv: 1412.3698 (2014)
64. Sonzogni A., McCutchan E.A., Johnson T.D., and Dimitriou P., *Effects of fission yield data in the calculation of antineutrino spectra for $^{235}\text{U}(n, \text{fission})$ at thermal and fast neutron energies, preprint (2015) and private communication*
65. Hayes A. C. et al. *Phys. Rev. D* 92:033015 (2015)
66. Vogel P., Schenter G. K., Mann F. M. and Schenter R. E, *Phys. Rev. C* 24:1543 (1981)
67. Dwyer D. A. and Langford T. J. *Phys. Rev. Lett.* 114:012502 (2015)
68. Hamsch F. -J., Knitter H. -H. and Budtz-Jorgensen C., *Nucl. Phys. A* 491, 56 (1989).

69. Sterbenz C., Louis W., Garvey G. Shaevitz M., CEU Poster, EA.00063, 2015 Fall Meeting of the APS Division of Nuclear Physics Volume 60, Number 13, (2015).
70. Aguilar A. *et al.*, *Phys. Rev. D* 64, 112007 (2001)
71. Aguilar-Arevalo A. *et al.*, *Phys.Rev.Lett.* 110 , 161801 (2013).
72. Abdurashitov J.N. *et al.*, *Phys. Rev. Lett.* 77, 4708 (1996), *Phys. Rev. C* 59, 2246 (1999), *Phys. Rev. C* 73 , 045805 (2006), and, *Phys. Rev. C* 80, 015807 (2009).
73. Anselmann P. *et al.*, *Phys. Lett. B* 342, 440 (1995), and Hampel W., *et al.*, *Phys. Lett. B* 420, 114 (1998), and Kaether F. *et al.* *Phys. Lett. B* 685 , 47 (2010)
74. Kopp J. *et al.* *JHEP* 1305:050 (2013)
75. Giunti C. *et al.* *Phys. Rev. D* 88:073008 (2013)
76. Abazajian K. N. *et al.* arXiv:1204.5379
77. Lasserre T. *TAUP 2013 Conference, F. Avignone and W. Haxton eds.*, arXiv 1404.7352 (2014)
78. Vogel P., Wen L.J. and Zhang C. *Nature Communications* 6:6935 (2015)
79. Gilje K, arXiv:1511.00177 (2015)
80. Ryder, *et al.*, arXiv:1510:07835 (2015), Moortgat C. arXiv:1511:07603 (2015).
81. Boireau G. *et al.*, arXiv:1509:05610 (2015)
82. Pequignot M. *Nucl. and Part. Phys. Proc.* 265:126 (2015)
83. Serebrov A. P. *et al.*, arXiv:1310:5521 (2013)
84. Derbin A. V., Kayunov A. S. and Muratova V. V. , arXiv:1204:2449 (2012)
85. Yeo I. S. *et al.* *J. Korean Phys. Soc.* 64:377 (2014)
86. Lane C. *et al.*, arXiv:1501.06935 (2015)
87. Alekseev I *et al.* *Phys. Part. Nucl. Lett.* 11:473 (2014)
88. Hollowayi S.T., Kawano T., and Möller P., *J. Korean Phys. Soc.* **59**, 875 (2011).
89. Kawano T., Moller P., and Wilson W.B., *Phys. Rev. C* **78**, 054601 (2008), and Kawano T. and Holloway S.T., “CGM: Cascading Gamma-ray and Multiplicity Code Ver. 3,” (2010) [unpublished].
90. Hardy J.C., Carraz L.C., Jonson B. and Hansen P.G., *Phys. Lett.* **71B**, 307 (1977).
91. ENSDF is the *Evaluated Nuclear Structure Data File*, compiled by the International Network of Nuclear Structure and Decay Data Evaluators (<http://www-nds.iaea.org/nsdd/>).
92. Dicus D. and Norton R.E., *Phys. Rev. D* 1, 1360 (1970).
93. Bottino A. and Chiocchetti, *Phys. Letts. B* 43, 170 (1973).
94. Armstrong L. and Kim C.W., *Phys. Rev. C* 5, 672 (1972).
95. Dickens J.K., Love T.A., McConnell J.W., and Peelle R.W., *Nucl. Sci. Eng.* **78**, 126 (1981).

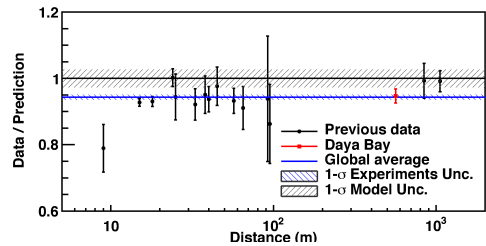


Figure 11

The measured reactor rate, normalized to the prediction of (19, 20) plotted as a function of the distance from the reactor core. The rate is corrected for the 3-flavor neutrino oscillation at each baseline. The data at the same baseline are combined for clarity. The Daya-Bay measurements are shown at the flux-weighted baseline (573 m) of the two near halls. Reproduced with permission from (61).